A Study of Total-Variation Based Noise-Reduction Algorithms For Low-Dose Cone-Beam Computed Tomography

Sovanlal Mukherjee   *sovaniitk@gmail.com*
Department of Radiation Oncology,
St. Jude Children's Research Hospital,
262 Danny Thomas Place,
Memphis, TN 38105, USA

Jonathan B. Farr   *Jonathan.Farr@stjude.org*
Department of Radiation Oncology,
St. Jude Children's Research Hospital,
262 Danny Thomas Place,
Memphis, TN 38105, USA

Weiguang Yao   *Weiguang.Yao@stjude.org*
Department of Radiation Oncology,
St. Jude Children's Research Hospital,
262 Danny Thomas Place,
Memphis, TN 38105, USA

Abstract

In low-dose cone-beam computed tomography, the reconstructed image is contaminated with excessive quantum noise. In this work, we examined the performance of two popular noise-reduction algorithms—total-variation based on the split Bregman (TVSB) and total-variation based on Nesterov's method (TVN)—on noisy imaging data from a computer-simulated Shepp–Logan phantom, a physical CATPHAN phantom and head-and-neck patient. Up to 15% Gaussian noise was added to the Shepp–Logan phantom. The CATPHAN phantom was scanned by a Varian OBI system with scanning parameters 100 kVp, 4 ms, and 20 mA. Images from the head-and-neck patient were generated by the same scanner, but with a 20-ms pulse time. The 4-ms low-dose image of the head-and-neck patient was simulated by adding Poisson noise to the 20-ms image. The performance of these two algorithms was quantitatively compared by computing the peak signal-to-noise ratio (PSNR), contrast-to-noise ratio (CNR) and the total computational time. For CATPHAN, PSNR improved by 2.3 dB and 3.1 dB with respect to the low-dose noisy image for the TVSB and TVN based methods, respectively. The maximum enhancement ratio of CNR for CATPHAN was 4.6 and 4.8 for TVSB and TVN respectively. For data for head-and-neck patient, the PSNR improvement was 2.7 dB and 3.4 dB for TVSB and TVN respectively. Convergence speed for the TVSB-based method was comparatively slower than TVN method. We conclude that TVN algorithm has more desirable properties than TVSB for image denoising.

Keywords: Low-Dose CBCT, Nesterov's First Order Method, Split Bregman Method, Total-Variation Method.

1. INTRODUCTION

Cone-beam computed tomography (CBCT) has been extensively used in radiation therapy to acquire high-resolution volumetric images of patients for treatment positioning [1-5]. However, CBCT uses ionizing X-ray radiation for imaging, which raises critical concerns about the risks associated with the extra radiation dose delivered to patients [6-8] because of the repeated use of CBCT during the treatment course. Current clinical protocols use a CBCT dose per scan of approximately 1 cGy for central tissues and a higher dose for most of the peripheral tissues [7,8]. Although the dose from a single scan is acceptable, the accumulation of doses over the treatment course (usually 4–6 weeks) can be substantial. The extra radiation exposure to normal tissue during

Sovanlal Mukherjee, Jonathan B. Farr & Weiguang Yao

CBCT increases the risk of cancer and genetic defects. Therefore, it is essential to minimize the unwanted CBCT radiation dose in order for patients to benefit from this modern medical imaging methodology.

The CBCT radiation dose can be reduced by minimizing the number of X-ray projections or reducing the product of the X-ray tube current and total exposure time (mAs). In CBCT, a filtered back-projection (FBP) algorithm originally proposed by Feldkamp, Davis, and Kress (FDK algorithm) [9-11] is widely adopted for image reconstruction from the projection. However, FDK-based CBCT reconstruction requires a sufficient number of X-ray projections. If the number of projections is inadequate, the FDK algorithm can cause aliasing artifacts in the reconstructed image because the Nyquist–Shannon sampling theorem is violated. For a reduced mAs, FDK reconstruction produces quantum noise in the images because of the reduced number of incident and detected photons. Both these properties of FDK-based algorithms are undesirable if a low-dose treatment procedure is required, especially for pediatric patients.

To overcome the artifact and noise problem imposed by FDK in low-dose imaging, various noise-reduction algorithms have been proposed, such as the penalized weighted least-squares (PWLS) method [12-14], total variation (TV)–based reconstruction [15-24] and the compressed sensing (CS) method [25-34]. Each of these algorithms is an optimization problem [35] that involves minimizing a cost or penalty function by using a standard iterative minimization routine.

In this study, we adopted TV-based noise-reduction algorithms to reduce the noise from low-dose imaging. The TV-based reconstruction proposed by Rudin, Osher, and Fatemi (ROF model) [15] was used to reduce noise from images contaminated by excessive noise. TV-based reconstruction works on the principle that minimizing the integral of the absolute gradient of an image, also known as the TV-norm of an image, reduces higher-frequency components such as streak artifacts and noise. Because the artifacts and noise usually exhibit a higher absolute gradient or TV, minimizing the gradient can help reduce the artifacts and noise [15].

The fundamental assumption of these TV-based algorithms is that the corresponding noise-free image is sparse. However, the noise property, scatter and beam hardening effect, and particularly the anatomical structures of CBCT images of patients challenge the sparseness assumption. It is therefore valuable to examine the performance of these algorithms on low-dose CBCT of patients. In this study, we applied TV-based algorithms to (1) a computer-generated Shepp–Logan phantom; (2) a physical CATPHAN phantom; and (3) imaging data from head-and-neck patient. Application to the Shepp-Logan phantom was mainly for the benchmark of the performance. In order to test the performance in highly noisy images of the CATPHAN phantom and patients, the images were from not only low mAs scanning but also the minimal slice thickness (0.38 mm). The TV-based image denoising algorithms were directly applied to the CBCT noisy reconstructed image. The performance of the algorithms was evaluated by the peak signal-to-noise ratio (PSNR), contrast-to-noise ratio (CNR) and the total computational time. For The physical CATPHAN phantom, imaging data was acquired by scanning the phantom with a Varian® cone-beam CT system with scanning parameters of 100 kVp, 20 mA, and 4 ms with full 644 projections. For clinical data, we used imaging data from head-and-neck patient. For the head-and-neck patient, the scanning parameters were 100 kVp, 20 mA, and 20 ms with 358 projections. The 4-ms imaging data from the head-and-neck patient was simulated by adding Poisson noise to the 20-ms imaging data. For the TV-based algorithm, the split Bregman method [22, 36] and Nesterov's first-order method [37, 38] were used to solve the minimization problem.

This paper is organized as follows. Section 2 describes the mathematical models of 3 noise-reduction algorithms. Section 2.1 describes TV-based reconstruction by using the split Bregman iteration technique. Section 2.2 presents the TV algorithm based on Nesterov's first-order method. Section 2.3 describes the mathematical model used to compute the PSNR and CNR. Sections 3 and 4 present the results and discussion, respectively, and Section 5 gives the conclusions.

2. METHODS

2.1 Total Variation Minimization using the Split Bregman Iterative Technique

The TV regularization technique was first studied by Rudin, Osher, and Fatemi [15] for denoising an image corrupted by Gaussian noise. Given a noisy image f and a denoised image g, the ROF model considers the solution of the following convex optimization problem:

$$\arg\min_{g} \quad \|g\|_{TV(\Omega)} + \frac{\lambda}{2}\int_{\Omega}(f(x)-g(x))^2 dx, \tag{1}$$

where λ is a positive parameter and $\|g\|_{TV(\Omega)}$ is the TV-norm of image g over a bounded region Ω and is defined by the integral of the gradient magnitude of g, given as

$$\|g\|_{TV(\Omega)} = \int_{\Omega}|\nabla g|dx \quad . \tag{2}$$

In the discretized form, equation (2) can be written as

$$\|g\|_{TV(\Omega)} \approx \sum_{i,j}\sqrt{(\nabla_x g)^2_{i,j} + (\nabla_y g)^2_{i,j} + \xi^2} \qquad i,j=1,2,3...N \ , \tag{3}$$

where ∇_x and ∇_y are discretized horizontal and vertical derivatives, respectively; ξ is a small positive parameter added to suppress singularity from the TV-norm; i and j are indices of pixels along the horizontal and vertical directions, respectively, of an $N \times N$ image; and N is the pixel size of the image. In equation (3), ∇_x and ∇_y are approximated by the finite difference scheme as

$$\begin{pmatrix}\nabla_x g_{i,j} \\ \nabla_y g_{i,j}\end{pmatrix} \approx \begin{pmatrix}g_{i+1,j} - g_{i,j} \\ g_{i,j+1} - g_{i,j}\end{pmatrix}. \tag{4}$$

TV minimization works on the principle that minimizing the gradient of an image reduces high-spatial-frequency components such as streaking artifacts and noise. More information about the ROF model is available in the literature [15, 40].

The ROF model was later modified by Goldstein and Osher [22] who adopted a split Bregman iteration scheme for solving the TV-regularized convex minimization problem. In this study, we applied the Goldstein and Osher model for image denoising by solving a constrained optimization problem of the following form [22]:

$$\arg\min_{d,g} \quad \sum_{i,j}|d_{i,j}| + \frac{\lambda}{2}\sum_{i,j}(f_{i,j}-g_{i,j})^2 + \frac{\gamma}{2}\sum_{i,j}|d_{i,j} - \nabla g_{i,j} - b_{i,j}|^2 \qquad i,j=1,2,3...N , \tag{5}$$

where d is the Bregman distance [22] and is given in equation (7); b is a variable related to the Bregman iteration; λ and γ are positive smooth and penalty parameters, respectively; and ∇g is the gradient of image g and is defined in equation (4).

Goldstein and Osher [22] solved equation (5) by using an alternating direction method, that is, minimizing g while keeping d fixed and vice versa. We followed the same approach for our study. According to the method of Goldstein and Osher [22], each step of the model can be summarized as follows:

Sovanlal Mukherjee, Jonathan B. Farr & Weiguang Yao

---

given tolerance $\delta > 0$, $\quad$ *paramaters* $\quad \lambda > 0, \gamma > 0$

Step 1: initialize $g^0 = 0, b^0 = 0, d^0 = 0$

for k=0,1,2…

Step 2 : *solve g subproblem*

$$\lambda g^{k+1} + \gamma \nabla^* \nabla g^{k+1} = \lambda f + \gamma \nabla^* (d^k - b^k) \tag{6}$$

Step 3: *solve d subproblem*

$$d^{k+1} = \frac{\nabla g^{k+1} + b^k}{\left| \nabla g^{k+1} + b^k \right|} * \max(\left| \nabla g^{k+1} + b^k \right| - \frac{1}{\gamma}, 0) \tag{7}$$

Step 4: *update b*

$$b^{k+1} = b^k + \nabla g^{k+1} - d^{k+1} \tag{8}$$

if $\left\| g^{k+1} - g^k \right\|_2 < \delta$

break; end

In equation (6), ∇^* is the transpose of the gradient operator ∇. In our study, equation (6) was solved by using the conjugate gradient method [41] because of its faster convergence.

2.2 Total Variation Minimization Using Nesterov's First-Order Method

In this study, we also solved the TV minimization problem using a different approach proposed by Nesterov in his seminal papers [37, 38]. We solved the TV minimization problem of the form

minimize $\left\| g \right\|_{TV}$

subject to $\left\| g - f \right\|_2 \leq \delta$ $\qquad\qquad\qquad$ (9)

In equation (9), *f* is the original noisy $N \times N$ image, *g* is the reconstructed denoised image, $\| \ \|_2$ is the l2-norm, and δ is the inconsistency tolerance between *f* and *g*.

Following Nesterov's method [37, 38], the optimization problem in equation (9) can be rewritten as the following saddle-point problem:

$$\min_{g \in Q_p} \max_{u \in Q_d} u^T \nabla g . \tag{10}$$

In equation (10), *T* is a transpose operator, and Q_p, Q_d are the primal and dual sets satisfying

$$Q_P = \left\{ g : \left\| g - f \right\|_2 \leq \delta \right\} \tag{11}$$

and

$$Q_d = \left\{ u : \left\| u_{ij} \right\|_2 \leq 1 \quad i = 1,2,3...N, j = 1,2,3...N \right\} \tag{12}$$

and u is a dual variable that can be defined by

$$u_{i,j}(g) = \max(\mu, \|\nabla g_{i,j}\|_2)^{-1} \nabla g_{i,j}.$$

(13)

In equation (13), ∇g is the gradient of g and can be solved by equation (4) and μ is a smoothing parameter.

Following Nesterov's approach, we smooth the following regularization function:

$$\Phi_\mu(g) = \max_{u \in Q_d} \left\{ u^T \nabla g - \frac{\mu}{2} \|u\|_2^2 \right\}$$

(14)

The gradient of (14) can be written as

$$\nabla \Phi_\mu(g) = \nabla^T u(g),$$

(15)

where ∇ is defined by

$$\nabla = \begin{pmatrix} \nabla_x \\ \nabla_y \end{pmatrix}.$$

(16)

∇_x, ∇_y of a function are defined in equation (4).

Finally, the overall Nesterov's algorithm can be summarized as follows:

---

given noisy data f, tolerance $\delta > 0$, smoothing parameter μ

set $g^0 = f$

for k=0,1,2…

find $G^k = \nabla \Phi_\mu(g^k)$

find $y^k = \arg\min_{g \in Q_p} \left\{ (g - g^k)^T G^k + \frac{L_\mu}{2} \|g - g^k\|_2^2 \right\}$ (17)

find $z^k = \arg\min_{g \in Q_p} \left\{ \frac{L_\mu}{2} \|g - f\|_2^2 + \sum_{i=0}^k \frac{i+1}{2} (g - g^i)^T G^i \right\}$ (18)

update $g^{k+1} = \frac{2}{k+3} z^k + \frac{k+1}{k+3} y^k$ (19)

if $\sum_{i=1}^N \sum_{j=1}^N \|\nabla g\|_2 + \delta \|\nabla^T u\|_2 - u^T \nabla f < threshold\ \varepsilon$ (20)

break

end

end

Following the variable transformation introduced by Dahl et al. [24], equations (17) and (18) can be solved as follows:

$$y^k = L_\mu(g^k - f) - G^k / \max(L_\mu, \left\| L_\mu(g^k - f) - G^k \right\|_2 / \delta) + f \tag{21}$$

and

$$z^k = -w^k / \max(L_\mu, \left\| w^k \right\|_2 / \delta) + f \tag{22}$$

where $w^k = \sum_{i=0}^{k} \frac{1}{2}(i+1)G^i$ and $L_\mu = \dfrac{\left\| \nabla \right\|_2^2}{\mu} \approx \dfrac{8}{\mu} =$ Lipschitz constant

For an $N \times N$ image,

$$\varepsilon = \left\| f \right\|_\infty N^2 \, 10^{-3}, \tag{23}$$

$$\mu = \frac{\varepsilon}{N^2}, \tag{24}$$

and

$$\delta = \tau N \sigma, \tag{25}$$

where σ is the standard deviation of the noise and τ is the smoothness parameter.

In the above steps, g^k is a vectored form, that is, the column-wise stacking of g for iteration k. The same holds true for y^k, z^k, G^k, and w^k. The original noisy image f was also vectored before applying Nesterov's algorithm.

2.3 Computation of the Peak Signal-to-Noise Ratio and the Contrast-to-Noise Ratio
In this study, for a quantitative comparison of the denoised images, the PSNR and CNR were computed. The PSNR was computed for the Shepp–Logan, CATPHAN phantom and clinical data from head-and-neck patients, and the CNR was computed for the CATPHAN phantom.

For an $N \times M$ image, the PSNR was computed using

$$\text{PSNR (dB)} = 10 \log_{10} \left(\frac{\max_f^2}{MSE} \right), \tag{26}$$

where $\max_f$ is the maximum pixel value of the reference image and

$$\text{MSE = mean square error =} \frac{1}{MN} \sum_{i=1}^{N} \sum_{j=1}^{M} [f(i, j) - g(i, j)]^2 . \tag{27}$$

In equation (27), f is the reference image and g is the reconstructed image. Because the PSNR is inversely proportional to the MSE, the low error between the reconstructed and reference image yields a higher PSNR.

In this study, the CNR was computed using [14]

$$CNR = \frac{|\mu_s - \mu_b|}{\sqrt{\sigma_s^2 + \sigma_b^2}} \; , \tag{28}$$

where μ_s and σ_s are the mean and standard deviation, respectively, of the pixel intensity at a region of interest (ROI) and μ_b and σ_b are the mean and standard deviation, respectively, of the pixel intensity at the background. Higher the CNR of a region within an image, higher is detectability of the region. In this study, the CNR was computed for the CATPHAN phantom.

3. RESULTS

In this section, we show the noise-reduced images of the Shepp–Logan phantom, the CATPHAN phantom, and head-and-neck images from the patient that was processed by the TVSB and TVN-based noise-reduction algorithms. The algorithms reduced noise from the FBP-reconstructed image. To compare the performance of the algorithms, the PSNR, CNR, and the total computational time was calculated.

3.1 Shepp–Logan Phantom Study

We studied the performance of the TVSB and TVN algorithms for a 512 × 512 two-dimensional (2D) Shepp–Logan phantom. For studying the algorithms, various levels of Gaussian noise were added to the original phantom. Figures 1(a)–(c) show the original 2D Shepp–Logan phantom. A 5%, 10%, and 15% Gaussian noise was added to the phantom, as shown in Figs. 1(d), (e), and (f) respectively. The denoised images obtained using the TVSB and TVN for individual noise levels are shown in Figs. 1(g)–(i) and 1(j)–(l), respectively. Figure 2 shows the line profiles of the original, noisy, and denoised phantoms for various noise levels. Tables 1 and 2 list the PSNR and the total computational time for TVSB and TVN methods respectively. For TVSB-based method, the improvement of PSNR was 15.10 dB, 16.10 dB, and 16.90 dB for 5, 10 and 15% noise respectively. For TVN, the corresponding improvement was 15.68 dB, 17.50 dB and 18.18 dB. The total computational time for TVN method was relatively lesser than TVSB as depicted by table 2.

3.2 CATPHAN Study

The performance of TVSB and TVN-based algorithms was also evaluated for a CATPHAN 504 phantom (The Phantom Laboratory, Salem, NY). The phantom was scanned by a calibrated On-board Imager (OBI) integrated with Trilogy (Varian Medical Systems, Palo Alto, CA).The flat panel aSi detector consists of 1024 × 768 pixels, and each pixel has a dimension of 0.38 mm × 0.38 mm. The phantom was scanned for a full 360 degrees, and 644 projections were acquired. The scanning parameters were the same as those routinely used in the clinic (i.e., 100 kV$_p$ and 20 mA), but pulse times of 4 ms and 32 ms were used for the low- and normal-dose images, respectively. Figure 3(a) shows the FBP-reconstructed image of CATPHAN for 644 projections with the scanning parameters of 100 kV$_p$, 20 mA, 32 ms, and reconstruction slice thickness 0.38 mm, and this image was considered as the normal-dose reference image. Figure 3(b) shows the FBP-reconstructed image of the same CATPHAN but with the scanning parameters of 100 kV$_p$, 20 mA, and 4 ms, and this image was considered as the low-dose noisy image. The 4-ms CATPHAN image was processed by using the TVSB and TVN methods, and the reconstructed images are shown in Figures 3(c) and (d) respectively. Table 3 lists the PSNR and computational time for the two algorithms for CATPHAN. The improvement of PSNR with respect to the noisy image was 2.3 and 3.1 dB respectively for TVSB and TVN based methods. The TVN method was computationally faster than TVSB as was depicted by table 2. The contrast-to-noise ratio (CNR) was computed at two regions of interest (ROI-1 and 2) for CATPHAN as shown in figure 3 (a). Table 4 lists the computed CNRs of the selected ROIs. For ROI-1, the CNR increased from 1.57 to 3.80 and 3.87 for TVSB and TVN method respectively. For ROI-2, the corresponding enhanced CNRs were 1.67 and 1.74 from 0.36.

3.3 Head-and-Neck Patient Study

For clinical data, images from a head-and-neck patient were acquired by using the Varian® OBI scanner at scanning parameters of 100 kV_p, 20 mA, 20 ms, and reconstruction slice thickness 0.38 mm. The detector consists of 1024 × 678 pixels, and patient data were acquired with 358 projections over 200 degrees. A full bow-tie filter was used for patient positioning. Figure 4(a) shows the FBP-reconstructed 20-ms image from the first head-and-neck patient, which was considered as a normal-dose reference image. Figure 4(b) shows the reconstructed 4-ms image that was simulated by adding the Poisson noise to the 20-ms image. Figures 4(c) and (d) show the reconstructed images processed by the TVSB and TVN methods, respectively. Table 5 lists the PSNRs and computational time for each algorithm for the head-and-neck data. The improvement of PSNR was 2.7 and 3.4 dB for TVSB and TVN based methods respectively. As for Shepp-Logan and CATPHAN, TVN method showed the same trend of faster computation than TVSB as was shown in table 5.

We also studied the effect of different regularization parameters pertaining to TVSB and TVN based methods and showed the processed denoised images for the head-and-neck data in figures 5 and 6 respectively.

4. DISCUSSION

Reconstructing a low-dose CBCT image is essentially a noise problem. FBP is a widely accepted analytical technique to reconstruct images from CBCT projection data, but it generates noise and sharp artifacts on the reconstructed images, especially when the mAs settings in the CBCT protocol are reduced. The reduced mAs settings are desired in the clinical protocol to reduce the radiation dose given to the patient. Various iterative reconstruction routines, such as the algebraic reconstruction technique (ART) [10,11], simultaneous-ART (SART) [10], PWLS [12-14], TV [16-21], and CS [28-34], have been proposed to reconstruct images from comparatively fewer projection data obtained from a reduced mAs settings. However, iterative algorithms are computationally more expensive and time consuming than FBP, and therefore translating these methods to radiation therapy in the clinical settings has been much debated. However, the computational time of the iterative algorithms can be reduced significantly by using graphic processing units (GPUs) parallel programming [46, 47].

In recent years, image denoising by using the TV [15-24] and CS [25-34] methods has been widely investigated. TV-based denoising is essentially a minimization problem wherein the gradient of an image function is minimized by using standard minimization methods, as was shown in equations (1), (5), and (9). In this study, we adopted the split Bregman method [22] and Nesterov's first order method [37, 38]. For validation, the algorithms were first applied to a digital Shepp–Logan phantom. The noise was reduced substantially as indicated by the reconstructed image, the proximity of the denoised line profile with the original profile, and a 15 to 18 dB improvement of the PSNR with respect to the noisy image. The convergence obtained using Nesterov's method was faster than that using the split Bregman method, as indicated by the computational time (Table 2). One potential reason for the higher computational time for TVSB based method is that the TVSB involves iterative conjugate gradient method as a technique to solve an intermediate step (eq. 6) as opposed to the analytical solution for all the intermediate steps in TVN.

The TV-based denoising method was also applied to a CATPHAN® phantom and data from head-and-neck patient. Noise was reduced in the reconstructed images, and there was a maximum 3.1 dB improvement of the PSNR with respect to the noisy image for CATPHAN. For the head-and-neck data, maximum PSNR improvement was 3.4 dB. To further evaluate the performance of TV-based algorithms, the CNR for a selected ROI was computed (Fig 3). For CATPHAN, ROI-1 and ROI-2 (ROI-1 having a higher contrast than ROI-2) were selected for CNR computation. By using TV-based methods, CNR enhancement ratios of 2.46 and 4.83 were obtained for ROI-1 and ROI-2, respectively, with respect to the noisy image (Table 4).

The CNRs computed by using TV-based algorithms were further compared with the CNRs from other noise reduction algorithms [14, 45] for CATPHAN as was listed in table 4.

The performance of TV-based algorithms largely depends on the selection of regularization parameters. In this study, the parameters were chosen on the basis of computation of the highest PSNR or CNR. Tables 6 and 7 list the individual parameters for the Shepp–Logan and CATPHAN phantoms and data from the head-and-neck patient. We showed the effect of different regularization parameters on the denoised images for the head-and-neck patient data in figures 5 and 6. An over-smoothing effect and loss of fidelity of the images was observed with an increasing regularization parameter as was shown in figures 5 and 6 for both the TVSB and TVN based methods.

In this study, in order to directly examine the performance of the algorithms, we have not used any noise-reduction filters prior to processing the CBCT reconstructed image through TV-based algorithms. Furthermore, 0.38 mm slice thickness was used in the reconstruction of the kV CBCT volumetric images to keep the highly noise level in the reconstructed slices. The noise level depends on the scanning parameter including mAs, the reconstruction parameters mainly the pixel size and slice thickness, and the reconstruction algorithm.

In this work, all computations were performed by using MATLAB® 8.1.0 in a Linux workstation with 32 GB of memory and an Intel® (core-i7) 3.4-GHz processor.

5. CONCLUSIONS

We implemented two noise-reduction algorithms TVSB and TVN to reduce the noise from low-dose CBCT images. The performance of the algorithms was evaluated by the reconstructed image, PSNR, CNR, and the computational time. An increase in the PSNR and CNR with respect to the noisy image supported the feasibility of these algorithms in reducing noise from low-dose images. In terms of noise reduction and total computational time, TVN-based methods performed better than TVSB.

6. REFERENCES

[1]   R.D. Timmerman, L. Xing. Image Guided and Adaptive Radiation Therapy, Philadelphia:Lippincott Williams and Wilkins, 2010.

[2]   D.A. Jaffray, J.S. Siewerdsen, J.W. Wong, A.A. Martinez. "Flatpanel cone-beam computed tomography for image-guided radiation therapy." Int. J. Radiat. Oncol. Biol. Phys., vol. 53, pp.1337–1349, 2002.

[3]   Y. Yang, E. Schreibmann, T.F. Li, C. Wang, L. Xing. "Evaluation of on-board kV cone beam CT (CBCT)-based dose calculation." Phys. Med. Biol., vol. 52, pp. 685–705, 2007.

[4]   L. Xing, B. Thorndyke, E. Schreibmann, Y. Yang, T.F. Li, G.Y. Kim, G. Luxton, A. Koong. "Overview of image-guided radiation therapy." Med. Dosim., vol. 31, pp. 91–112 , 2006.

[5]   D.A. Jaffray. "Emergent technologies for 3-dimensional image-guided radiation delivery." Semin. Radiat. Oncol., vol.15, pp. 208–216, 2005.

[6]   Murphy et al. "The management of imaging dose during image guided radiotherapy: Report of the AAPM Task Group 75." Med. Phys., vol. 34, pp. 4041–4063, 2007.

[7]   D.J. Brenner, E.J. Hall. "Computed tomography-An increasing source of radiation exposure." N. Engl. J. Med., vol. 357, pp. 2277–2284, 2007.

[8]   Wen et al. "Dose delivered from Varian's CBCT to patients receiving IMRT for prostate cancer." Phys. Med. Biol., vol. 52, pp. 2267–2276, 2007.

[9]   L.A. Feldkamp, L.C. Davis, J.W. Kress. "Practical cone-beam algorithm." J. Opt. Soc. Am. A., vol. 1, pp. 612–619, 1984.

[10] A.C. Kak and M Slaney. Principles of computerized tomographic imaging. New York: IEEE Press,1988.

[11] G.T. Herman. Image Reconstruction from Projections: The Fundamentals of Computerized Tomography. New York: Academic Press, 1980.

[12] J. A. Fessler. "Penalized weighted least-squares image reconstruction for Positron emission Tomography." IEEE Trans. Med. Imag., vol. 13, pp. 290–300, 1994.

[13] J. Wang, T. Li, H. Lu, Z. Liang. "Penalized weighted least-squares approach to sinogram noise reduction and image reconstruction for low-dose X-ray computed tomography." IEEE Trans. Med. Imag., vol. 25, pp.1272–83, 2006.

[14] J. Wang, T. Li, Z. Liang, L. Xing. "Dose reduction for kilovoltage cone-beam computed tomography in radiation therapy." Phys. Med. Biol., vol. 53, pp. 2897–2909, 2008.

[15] L.I. Rudin, S. Osher, E. Fatemi. "Nonlinear total variation based noise removal algorithms." Physica D, vol. 60, pp. 259–268, 1992.

[16] E.Y. Sidky, C.M. Kao, X. Pan. "Accurate image reconstruction from few-views and limited angle data in divergent-beam CT." J. X-Ray Sci. Technol., vol. 14, pp. 119–39, 2006.

[17] E.Y. Sidky, X. Pan. "Image reconstruction in circular cone-beam computed tomography by constrained, total-variation minimization." Phys. Med. Biol., vol. 53, pp. 4777–4807, 2008.

[18] E.Y. Sidky, Y. Duchin, X. Pan, C. Ullberg. "A constrained, total-variation minimization algorithm for low-intensity x-ray CT." Med. Phys., vol. 38, pp. 117–25, 2011.

[19] Z. Tian, X. Jia, K. Yuan, T. Pan, S.B. Jiang. "Low-dose CT reconstruction via edge-preserving total variation regularization." Phys. Med. Biol., vol. 56, pp. 5949–5967, 2011.

[20] Z. Chen, X. Jin, L. Li, G. Wang. "A limited-angle CT reconstruction method based on anisotropic TV minimization." Phys. Med. Biol., vol. 58, pp. 2119–2141, 2013.

[21] L. Ritschl, F. Bergner, C. Fleischmann, M. Kachelriess. "Improved total variation-based CT image reconstruction applied to clinical data." Phys. Med. Biol., vol. 56, pp. 1545-61, 2011.

[22] T. Goldstein, S. Osher. "The Split Bregman Method for L1 Regularized Problems." SIAM J. Imag. Sci.,vol. 2, pp. 323–343, 2009.

[23] A. Chambolle. "An Algorithm for Total Variation Minimization and Applications." J.Math. Imag. Vis., vol. 20, pp. 1-2, 2004.

[24] J. Dahl, P.C. Hansen, S.H. Jensen, T.L. Jensen. "Algorithms and software for total variation image reconstruction via first-order methods." Numer. Algor., vol. 53, pp. 67–92, 2010.

[25] E.J. Candes, J. Romberg, T. Tao. "Robust uncertainty principles: Exact signal reconstruction from highly incomplete frequency information." IEEE Trans. Inf. Theory, vol. 52, pp. 489–509, 2006.

[26] E.J. Candes, T. Tao. "Near-optimal signal recovery from random projections: Universal encoding strategies." IEEE Trans. Inf. Theory, vol. 52, pp. 5406–5425, 2006.

[27] D.L. Donoho, "Compressed sensing." IEEE Trans. Inf. Theory, vol. 52, pp. 1289–1306, 2006.

[28] G. Chen, J. Tang, S. Leng. "Prior image constrained compressed sensing (PICCS): A method to accurately reconstruct dynamic CT images from highly undersampled projection data sets." Med. Phys., vol. 35, pp. 660–663, 2008.

[29] J. Tang, B.E. Nett, G. Chen. "Performance comparison between total variation (TV)-based compressed sensing and statistical iterative reconstruction algorithms." Phys. Med. Biol., vol. 54, pp. 5781–5804, 2009.

[30] S. Becker, J. Bobin, E.J. Candes. "NESTA: a fast and accurate first-order method for sparse recovery." SIAM J. Imag. Sci., vol. 4, pp. 1–39, 2009.

[31] K. Choi, J. Wang, L. Zhu, T.S. Suh, S. Boyd, L. Xing. "Compressed sensing based cone-beam computed tomography reconstruction with a first-order method." Med. Phys., vol. 37, pp. 5113–5125, 2010.

[32] J. Park, B. Song, J. Kim, S. Park, H. Kim, Z. Liu, T. Suh, W. Song. "Fast compressed sensing-based CBCT reconstruction using Barzilai–Borwein formulation for application to on-line IGRT." Med. Phys., vol. 39, pp. 1207–17, 2012.

[33] T. Niu, L. Zhu. "Accelerated barrier optimization compressed sensing (ABOCS) reconstruction for cone-beam CT: Phantom studies." Med. Phys., vol. 39, pp. 4588-98, 2012.

[34] Niu et al. "Accelerated barrier optimization compressed sensing (ABOCS) for CT reconstruction with improved convergence." Phys. Med. Biol., vol. 59, pp. 1801-14, 2014.

[35] S.P. Boyd, L. Vandenberghe. Convex Optimization. Cambridge: Cambridge University Press, 2004.

[36] L.M. Bregman. "The relaxation method of finding the common points of convex sets and its application to the solution of problems in convex optimization." USSR Comp. Math. & Math. Phys., vol. 7, pp. 200–217, 1967.

[37] Y. Nesterov. "Gradient methods for minimizing composite objective function. Center for Operations Research and Econometrics (CORE)." Universite Catholique de Louvain, Tech. Rep., 2007.

[38] Y. Nesterov. "A method for unconstrained convex minimization problem with the rate of convergence O (1/k2)." Sov. Math. Dokl., vol. 27, pp. 372–376, 1983.

[39] J. Barzilai, J.M. Borwein. "2-Point step size gradient methods." IMA J. Numer. Anal., vol. 8, pp. 141–148, 1988.

[40] P. Getreuer. "Rudin–Osher–Fatemi Total Variation Denoising using Split Bregman." Imag. Proc. vol. 2, pp. 74–95, 2012.

[41] P. Sonneveld. "CGS: A fast Lanczos-type solver for nonsymmetric linear systems." SIAM J. Sci. Stat. Comput., vol. 10, pp. 36-52, 1989.

[42] H.H. Bauschke, J.M. Borwein. "On Projection algorithms for solving convex feasibility problems." SIAM Review, vol. 38, pp. 367-426, 1996.

[43] S. Osher, M. Burger, D. Goldfarb, J.J. Xu, W.T. Yin. "An iterative regularization method for total variation-based image restoration." Multiscale Model. Simul., vol. 4, pp. 460–489, 2005.

[44] W. Yin, S. Osher, D. Goldfarb, J. Darbon. "Bregman iterative algorithms for l1-minimization with applications to compressed sensing." SIAM J. Imaging Sci., vol. 1, pp.143–168 2008.

[45] W. Yao, J.B. Farr. "A multiscale filter for noise reduction of low-dose cone beam projections." Phys. Med. Biol., vol. 60, pp. 6515–6530, 2015.

[46] F. Xu, K. Mueller. "Real-time 3D computed tomographic reconstruction using commodity graphics hardware." Phys. Med. Biol., vol. 52, pp. 3405–3419, 2007.

[47] Jia et al. "GPU-based fast low-dose cone beam CT reconstruction via total variation." J. X-Ray Sci. Technol., vol. 19, pp.139–154, 2011.
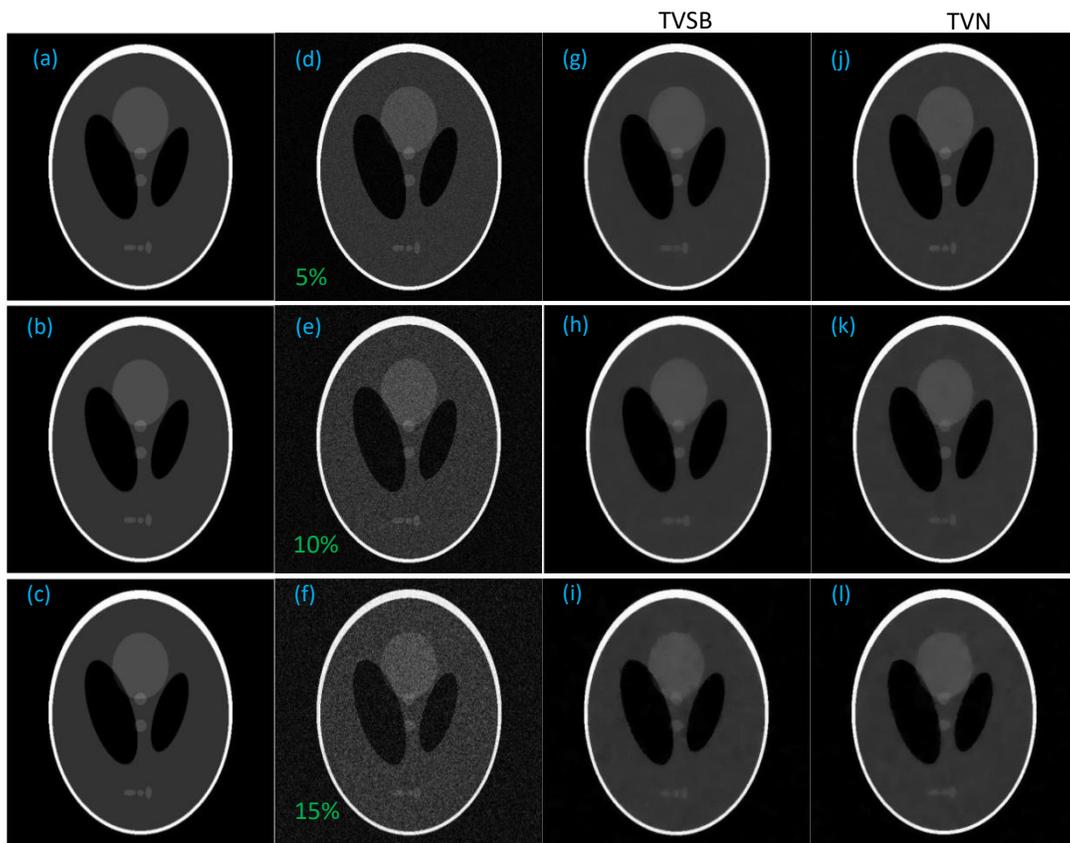
APPENDIX

FIGURE 1: (a) ,(b) and (c) Original 512 x 512 Shepp-Logan Phantom, (d) ,(e) and (f) 5%, 10% and 15% additive Gaussian noise added to the phantom respectively, (g), (h) and (i) Respective denoised images using TVSB, (j),(k), and (l) Respective denoised images using TVN.
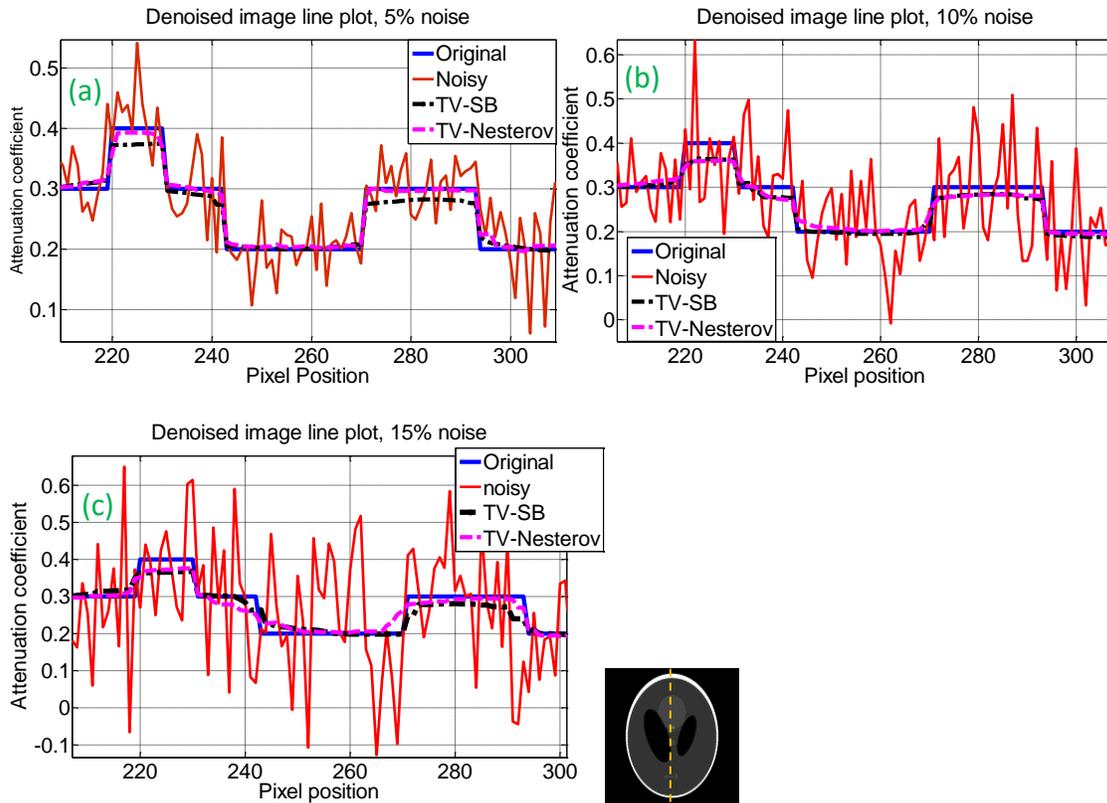
FIGURE 2: (a) , (b) and (c): Line profiles of original, noisy and denoised Shepp-Logan phantom for 5%, 10% and 15% Gaussian noise respectively. The line profile was plotted across the dashed yellow vertical line shown on the phantom image.
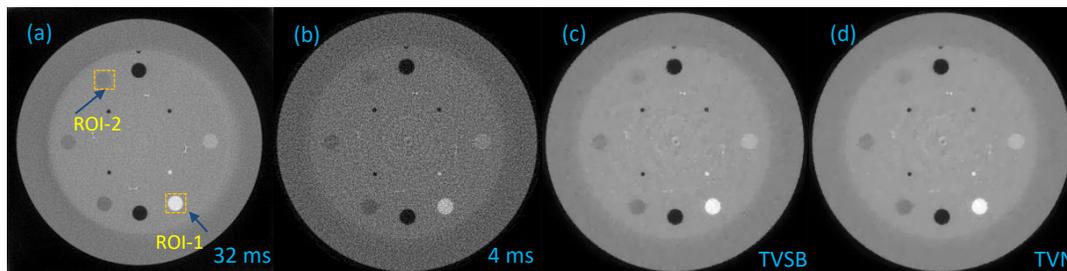

FIGURE 3: (a) Scanned CATPHAN image with the scanning parameters of 100 kV$_P$, 20 mA and 32 ms (used as a "Gold Standard" image), (b): Same CATPHAN scanned with 4 ms (used as a low-dose noisy image), (c) and (d) Processed 4 ms CATPHAN image through TVSB and TVN algorithm respectively. Regions of interest (ROIs) for computing the CNRs were shown in Fig. 3(a).
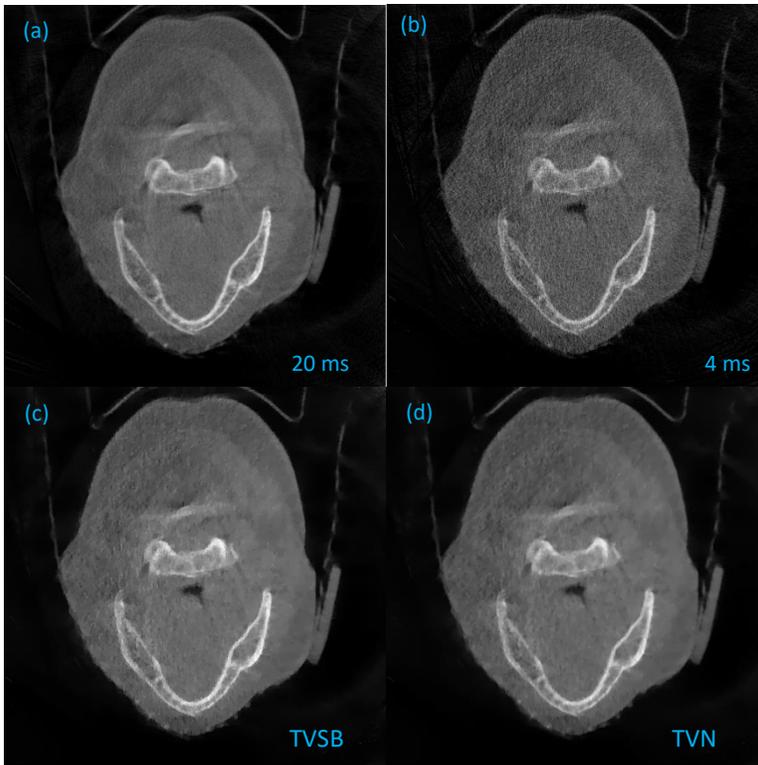
FIGURE 4: (a) Scanned imaging data from the head-and-neck patient with the scanning parameters of 100 kV_P, 20 mA and 20 ms (used as "Gold Standard" image), (b) Same data scanned with 4 ms pulse time (used as a low-dose noisy image), (c) and (d) Processed 4 ms data through TVSB and TVN algorithm respectively.
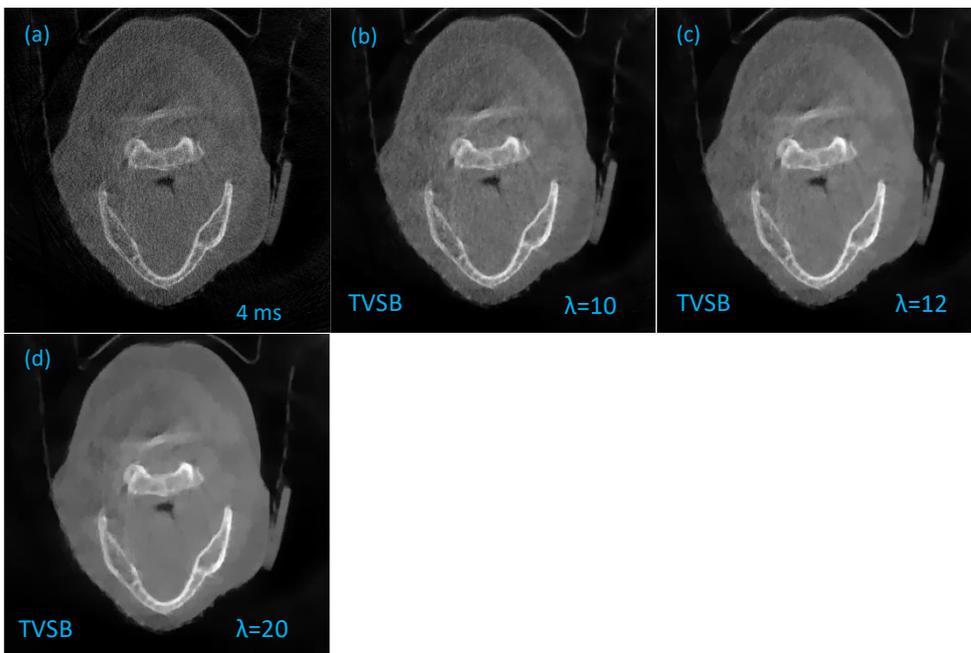

FIGURE 5: (a) Scanned imaging data from the head-and-neck patient with the scanning parameters of 100 kV_P, 20 mA and 4 ms (used as "noisy" image), (b) and (c) Processed 4 ms data through TVSB algorithm for three different regularization parameters.

FIGURE 6: (a) Imaging data from the head-and-neck patient with the scanning parameters of 100 kV$_P$, 20 mA and 4 ms (used as "noisy" image), (b) and (c) Processed 4 ms data through TVN algorithm for three different regularization parameters.
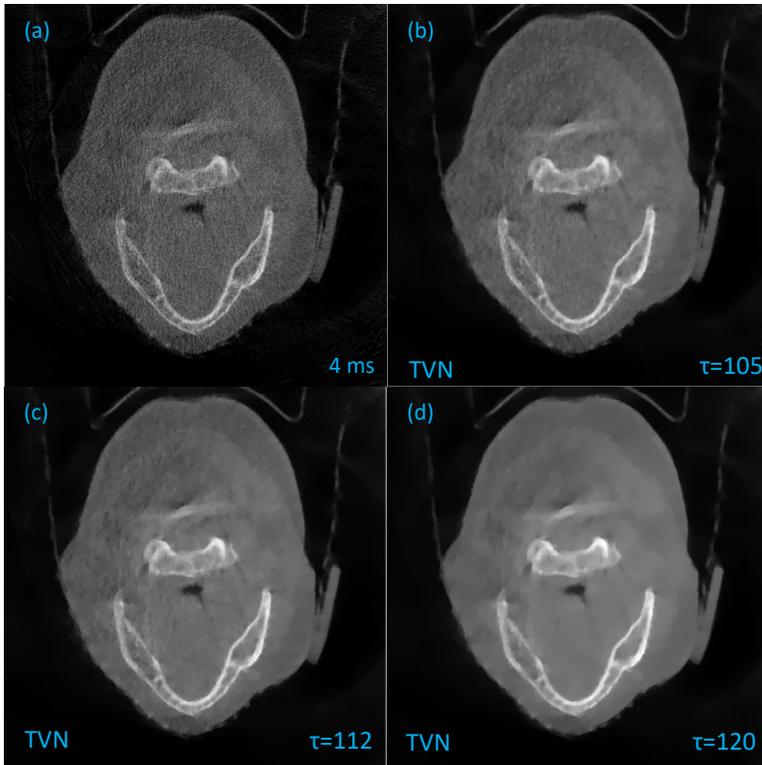
Noise level (%)	PSNR (Noisy) (dB)	PSNR (TVSB) (dB)	PSNR (TVN) (dB)
5	26.02	41.20	41.70
10	20.00	36.10	37.50
15	16.40	33.30	34.50

TABLE 1: Peak signal-to-noise ratio (PSNR) for Shepp-Logan phantom with different levels of added Gaussian noise.

Noise level (%)	Computional time (TVSB) (s)	Computational time (TVN) (s)
5	10	5
10	11	8
15	14	10

TABLE 2: Peak signal-to-noise ratio (PSNR) for Shepp-Logan phantom with different levels of added Gaussian noise.

Parameter	Noisy image (4 ms)	TVSB	TVN
PSNR(dB)	15.6	17.9	18.7
Computation time (s)	-	11.1	7

TABLE 3: Peak signal-to-noise ratios (PSNRs) and computational time for CATPHAN.

Parameter	Noisy image (4 ms)	TVSB	TVN	$\dfrac{CNR_{max}}{CNR_{noisy}}$	$\dfrac{CNR_{max}}{CNR_{noisy}}$ [Ref. 45]	$\dfrac{CNR_{max}}{CNR_{noisy}}$ [Ref. 14]
CNR(ROI-1)	1.57	3.80	3.87	2.46	3.4	2.8
CNR(ROI-2)	0.36	1.68	1.74	4.8	4.47	2.47

TABLE 4: Contrast-to-noise ratios (CNRs) for CATPHAN.

Parameter	Noisy image (4 ms)	TVSB	TVN
PSNR(dB)	25.5	28.2	28.9
Computation time (s)	-	14.1	9

TABLE 5: Peak signal-to-noise ratios (PSNRs) and computational time for head-and-neck patient data.

Noise level (%)	TVSB	TVN
5	λ=0.08, γ=1	τ=0.98
10	λ=0.10, γ=1	τ=0.98
15	λ=0.14, γ=1	τ=0.98

TABLE 6: Parameters of TVSB and TVN for Shepp-Logan phantom.

Imaging Data	TVSB	TVN
CATPHAN	λ=20, γ=1	τ=180
Head-and-Neck	λ=10, γ=1	τ=105

TABLE 7: Parameters for CATPHAN and Head-and-Neck data.